

1 **Parametric subharmonic instability of the internal tide at 29N**

2 **J. A. MACKINNON ***

Scripps Institution of Oceanography, La Jolla, CA, USA

3 **M. H. ALFORD**

Applied Physics Laboratory and School of Oceanography, University of Washington, Seattle, WA, USA

4 **OLIVER SUN**

Woods Hole Oceanographic Institution, Woods Hole, MA, USA

5 **ROB PINKEL**

Scripps Institution of Oceanography, La Jolla, CA, USA

6 **ZHONGXIANG ZHAO**

Applied Physics Laboratory, University of Washington, Seattle, WA, USA

7 **JODY KLYMAK**

University of Victoria, Victoria, British Columbia, Canada

*E-mail: jmackinn@ucsd.edu

ABSTRACT

9 Observational evidence is presented for transfer of energy from the internal tide to near-
10 inertial motions near 29°N in the Pacific Ocean. The transfer is accomplished via paramet-
11 ric subharmonic instability (PSI), which involves interaction between a primary wave (the
12 internal tide in this case) to two smaller-scale waves of near half the frequency. The inter-
13 nal tide at this location is a complex superposition of a low-mode waves propagating north
14 from Hawaii and higher-mode waves generated at local seamounts, making application of
15 PSI theory challenging. Nevertheless, a statistically significant phase locking is documented
16 between the internal tide, and upward and downward-propagating near-inertial waves. The
17 phase between those three waves are consistent with that expected from PSI theory. Cal-
18 culated energy transfer rates from the tide to near-inertial motions are modest, consistent
19 with local dissipation rate estimates. The conclusion is that while PSI does befall the tide
20 near a critical latitude of 29°N , it does not do so catastrophically.

21 1. Introduction

22 *Motivation*

23 Internal tides provide one of the major dynamical pathways from large-scale energy in
24 the ocean to small-scale turbulent dissipation and mixing. Internal tide generation occurs
25 where the barotropic tide interacts with rough topography, the global patterns of which are
26 relatively well known (Nycander 2005; Garrett and Kunze 2007). However the geography
27 of internal tide dissipation is not well quantified, mostly due to a lack of understanding of
28 the waves' propagation and dynamical processes leading to wave breaking. Given that both
29 regional and global climate models are sensitive to the distribution of the resultant diapycnal
30 mixing (Harrison and Hallberg 2008; Jochum 2009; Jayne 2009), investigating the fate of the
31 internal tide is a priority of the field.

32 The Internal Waves Across the Pacific (IWAP) experiment was designed in part to test
33 the hypothesis that the tide loses significant energy through parametric subharmonic in-
34 stability (PSI) near a critical latitude of 29°N , as predicted by the numerical simulation
35 of MacKinnon and Winters (2005) (hereafter MW). PSI involves transfer of energy from
36 a propagating low-mode wave to two smaller-scale waves near half the frequency through
37 nonlinear interaction (Müller et al. 1986). It has been documented near sites of both strong
38 semidiurnal internal tides (Carter and Gregg 2006; Alford et al. 2007; Sun 2010) and diurnal
39 internal tides (Alford 2008). MW suggested this mechanism would be particularly effective
40 near 29N , where the half-frequency 'daughter' waves are close to the local inertial frequency,
41 a natural resonant frequency of the ocean. Though the MW results showed catastrophic
42 tidal decay, Hazewinkel and Winters (2011) note that expected PSI growth rates are often
43 comparable to the timescales over which internal tides vary (spring-neap or otherwise), which
44 may provide a natural upper bound to total instability growth.

45 Strong PSI could potentially be an important part of the global pattern of diapycnal
46 mixing. Subharmonic waves tend to have smaller vertical scales (higher shear) and slow

47 group velocities, making them likely to dissipate nearby. Simmons (2008) sees just such an
 48 effect in a global numerical simulation of the semidiurnal internal tide, although it less of a
 49 band than a series of localized mixing patches where strong internal tide beams cross 29 N or
 50 S. Additionally, any internal tide energy lost to PSI is not available to dissipate elsewhere in
 51 the ocean, so any attempt a a global internal tide energy budget must take PSI into account.

52 *Basic Theory*

53 Nonlinear energy transfer between internal waves has often been conceptualized with
 54 resonant wave-wave interaction theory. In this view, energy is transferred between a triad
 55 of weakly nonlinear waves through the first order term of a perturbation expansion in wave
 56 amplitude (McComas 1977; Olbers 1983; Müller et al. 1986). The dynamical terms respon-
 57 sible for energy transfer are the quadratic terms in the equations of motion ($\mathbf{u} \cdot \nabla \mathbf{u}$, etc).
 58 The interaction is strongest when participating wavenumbers and frequencies satisfy simple
 59 resonance conditions,

$$60 \quad \omega_1 \pm \omega_2 = \omega_0; \quad \mathbf{k}_1 \pm \mathbf{k}_2 = \mathbf{k}_0 \quad (1)$$

61 PSI refers to a subset of such interactions where the two so-called daughter waves (ω_1, ω_2)
 62 are both near half the frequency of the primary wave (ω_0). The interaction is thought to be
 63 particularly resonant at the latitude at which the half-frequency motions are exactly inertial
 64 (MW, Young et al. (2008)), which we refer to as a critical latitude, as it is a critical or turning
 65 latitude for the subharmonic (diurnal) waves. Unlike wind-generated near-inertial internal
 66 waves, which typically propagate downwards from the surface, the daughter waves created
 67 by PSI have both up and down-going energy. At this latitude (28.8 for the dominant M_2
 68 internal tide and 29.9 for the secondary S_2 internal tide), the daughter waves are very close
 69 to inertial, and hence are expected to have vanishing vertical velocities and displacements.
 70 As a result, most of the quadratic energy transfer terms drop out, resulting in a relatively

71 simple expression for energy input into one of the daughter waves:

$$72 \quad \frac{\partial E_1}{\partial t} = -u_1^*[u_2^* \frac{\partial u_0}{\partial x} + v_2 \frac{\partial u_0}{\partial y}] - v_1^*[u_2^* \frac{\partial v_0}{\partial x} + v_2^* \frac{\partial v_0}{\partial y}] + c.c. \quad (2)$$

73 where the stars indicate complex conjugates, $E_1 = (u_1 u_1^* + v_1 v_1^*)/2$, and ‘c.c’ denotes
 74 the complex conjugate of the whole expression, necessary to get a real energy transfer. An
 75 equivalent expression is found in Young et al. (2008) who pose the problem more generally
 76 as near-inertial instabilities of a horizontally uniform current oscillating at twice the local
 77 inertial frequency. Physically, (2) states that subharmonic motions draw energy from hori-
 78 zontal gradients in the primary wave, in this case the internal tide (MW). As Young et al.
 79 (2008) point out, this is at odds with a common dynamical view of PSI as forced by periodic
 80 modification of the buoyancy frequency by internal tide strain, though such a mechanism
 81 may be in play at lower latitudes.

82 When considered in a frame of reference aligned with the direction of propagation of the
 83 internal tide, (2) simplifies further to

$$84 \quad \frac{\partial E_1}{\partial t} = -\frac{3}{2} i k_0 u_1' u_2'^* u_0 + c.c. \quad (3)$$

85 where k_0 is the horizontal wavenumber of the internal tide and primed velocity and u' ,
 86 indicates horizontal velocity in the direction of internal tide propagation.

87 Before attempting to apply (3) to the data, we note several salient features. First, since
 88 the waves must satisfy wavenumber as well as frequency resonance, daughter waves with
 89 smaller vertical scales than the primary wave must have vertical wavenumbers of opposite
 90 signs. In other words, we expect one near-inertial daughter wave (u_1 or u_2) with phase that
 91 propagates upwards in time, and one with downwards phase propagation. This supposition
 92 will be exploited in simplifying the data analysis below. Second, it is impossible to directly
 93 calculate the horizontal internal tide wavenumber in (3) from time series data at a single
 94 location. A helpful step is to use the linear internal wave polarization relations to replace
 95 the horizontal internal tide velocity (u_0) with vertical internal tide velocity (w_0),

$$96 \quad \frac{\partial E_1}{\partial t} = \frac{3}{2} i m_0 u_1' u_2'^* w_0 + c.c. \quad (4)$$

97 where m_0 is now the vertical wavenumber of the internal tide. However, even though the
 98 internal tide horizontal wavenumber no longer explicitly appears, the crucial fact remains
 99 that (4) must be applied in a reference frame aligned with the propagation direction of
 100 the tide. This factor can be made explicit by rewriting the equation in terms of cardinal
 101 velocities

$$\begin{aligned}
 102 \quad \frac{\partial E_1}{\partial t} &= \frac{3}{2} m_0 \mathbf{u}_1^* \mathbf{u}_2^* w_0 e^{i(2\theta_k + \pi/2)} + c.c. \\
 103 \quad &\equiv \Gamma e^{i(2\theta_k + \pi/2)} + c.c. \\
 104 \quad &\equiv |\Gamma| e^{i\theta_\Gamma} e^{i(2\theta_k + \pi/2)} + c.c. \tag{5}
 \end{aligned}$$

105 where θ_k is defined here to be the horizontal propagation direction of the internal tide CCW
 106 from due East, and $\mathbf{u}^* = (u + iv)^*$ where (u, v) are eastward and northward velocities.
 107 The factor of 2 in front of θ_k arises because both daughter wave velocities must go through
 108 coordinate frame rotation. For convenience we have separated out a triple product term (Γ)
 109 and terms involving angles, including the factor of i from (4). θ_Γ is the complex phase of
 110 the triple product Γ . Physically, there is a net energy transfer from the primary wave (the
 111 internal tide) to two subharmonic waves when (5) is positive. The term is maximized if the
 112 complex phase of the triple product, Γ cancels the multiplying term,

$$113 \quad \theta_\Gamma = -(2\theta_k + \pi/2) \tag{6}$$

114 The rate or strength of energy transfer depends on the magnitude of Γ averaged over
 115 time; non negligible time-averaged energy transfer occurs only if the three terms involved
 116 maintain a consistent sense of relative phase in time. Below we demonstrate that both of
 117 these requirements, a consistent triple product phase and a particular phase satisfying (6),
 118 are satisfied by the present data.

120 Here we present detailed evidence for PSI where an internal tide propagating north from
121 Hawaii crosses 29N. Preliminary results in Alford et al. (2007) (hereafter A07) demonstrated
122 that while there was clear evidence of PSI near 29N, it did not catastrophically drain energy
123 from the internal tide. Zhao et al. (2010) show further that the internal tide propagates
124 significantly further north without substantial loss of energy. Here we document the inter-
125 action between the internal tide and local high-mode near-inertial waves at 29N, showing
126 consistent phasing and positive, yet modest, estimated rates of energy transfer. Estimates
127 of turbulent mixing rates are presented in a companion paper (MacKinnon et al. 2012). The
128 remainder of the paper is organized as follows: Section 2 describes the basic experimental
129 design, Section 3 describes basic properties of both near-inertial and semi-diurnal waves,
130 Section 4 documents evidence for energy transfer between the two, and Section 5 presents a
131 discussion of results.

132 **2. Experimental design**

133 A series of observations were made during two cruises aboard *R/V Revelle* during spring
134 2006 spanning 60 days and 12 degrees of latitude (Fig. 1) (see the companion paper and A07
135 for more details). Here we focus on a 50-day moored time series at 28.9N, mooring MP3,
136 collected from 25 April to 13 June 2006. A McLane Moored Profiler on the mooring crawled
137 from 85-1400 m every 1.5 hours each way, measuring temperature, salinity, and horizontal
138 velocity (Doherty et al. 1999). The profiler was equipped with an Acoustic Current Meter
139 and CTD from Falmouth Scientific. Corrections were made for mis-matched temperature and
140 conductivity cells following Lueck and Picklo (1990). In order to remove residual sensor noise,
141 temperature and conductivity data were smoothed to 3 m. Velocity data were smoothed to
142 10 meters (increased noise associated with profiler motion begins to dominate at smaller
143 scales, Alford (2010)). A now-known firmware bug caused the profiler to go to sleep on May

144 10 (yearday 129), resulting in a one-day data gap for all variables.

145 All data were put into a semi-Lagrangian reference frame by referencing measurements on
146 each isopycnal to the average resting depth of that isopycnal (Fig. 2). Vertical displacements
147 were calculated by subtracting the time-mean density profile and dividing by a smoothed
148 average buoyancy frequency profile. Vertical velocity was computed by time-differencing
149 vertical displacement (Pinkel et al. 2012).

150 3. Observed wave properties

151 Velocity at MP3 is dominated by a combination of diurnal and semidiurnal signals (Fig.
152 2). Kinetic energy spectra show a large peak near the local inertial frequency and two
153 distinct semidiurnal peaks at M_2 and S_2 (Fig. 3). For simplicity we refer to semidiurnal
154 motions using the label D_2 . As previously mentioned, the subharmonic frequency ($D_2/2$)
155 is close to the local inertial frequency at this latitude, so the inertial shear may include a
156 combination of PSI and wind-generated motions (Pickering et al. 2012). Before looking for
157 evidence of nonlinear wave interactions, we separately discuss properties of the near-inertial
158 and semidiurnal motions. In each case data have been bandpassed in the relevant frequency
159 band with a fourth order Butterworth filter with passbands of $[0.8-1.3] \times f$ or M_2 .

160 *Near-inertial waves*

161 Bandpassed near-inertial velocity shows a series of wave groups, as documented in more
162 detail by Pickering et al. (2012) (Fig. 4). As described by A07, there are several periods
163 with a ‘checkerboard’ pattern of near-inertial velocity (e.g. near 600 m depth between year-
164 days 120 and 125), indicating the sum of up-going and down-going waves. At other times
165 (near 1000 m depth and yearday 155) phase clearly propagates upward in time, consistent
166 with downward energy propagation. Near-inertial motions can be decomposed into motions
167 that rotate CW and CCW with increasing depth by taking positive and negative quadrants

168 of vertical Fourier transforms of $(u + iv)$ at each point in time. According to the linear
169 internal-wave polarization relations, a sense of CW rotation with increasing depth is consis-
170 tent with phase that propagates upward with time (downward energy propagation), while
171 CCW rotation is consistent with downward phase and upward energy propagation (Leaman
172 and Sanford 1976). On average, there is comparable energy in motions with upward and
173 downward phase (blue versus red in Fig. 3). Figure 4 (bottom two panels) shows the decom-
174 posed velocity fields. The observed sense of phase propagation with time for each one (i.e. up
175 for CW and down for CCW) is indeed consistent with expectations, suggesting motions that
176 can be considered quasi-linear internal waves. Over the 50 days of mooring measurement,
177 multiple wave groups are clearly present. A run length test of either upward or downward
178 near-inertial energy shows they are uncorrelated at timescales of 2.5 days or longer at the 5%
179 level of significance (Gregg et al. 2003), a value that will be used in statistical significance
180 calculations below .

181 *Semi-diurnal waves*

182 The internal tide at 29N is a complex superposition of waves propagating different direc-
183 tions. Zhao et al. (2010) show that though there is a coherent north-bound mode-one tide
184 at the southernmost mooring (MP1), the further north one goes from the generation site
185 the more complicated things become. In particular, at the latitude of MP3, the data shows
186 comparatively larger amplitudes for higher modes (Zhao et al. 2010). A regional numerical
187 internal tide simulation made with the POM model suggests higher mode internal tides have
188 complex spatial structure, with some energy radiating from the local Musicians Seamounts.
189 For example, modeled mode-3 fluxes show a pulse of energy propagating to the northwest
190 near the mooring location (Fig. 6), although flux direction is highly variable near the moor-
191 ing location. Given that these waves are expected to be significantly refracted by an evolving
192 mesoscale (Rainville and Pinkel 2006), an effect not included in the POM model, detailed
193 point comparisons between modeled and observed data are not pursued further here.

194 The complex depth and time structure of semidiurnal bandpassed velocity is shown in
 195 Figure 5. There are several periods of relatively large north-south velocity, roughly consistent
 196 with the average northward energy flux observed at this site (vectors in Fig. 1). However,
 197 while internal tide flux is generally dominated by low modes, we expected motions with
 198 higher horizontal wavenumbers to contribute more to PSI (3). For linear internal waves the
 199 horizontal wavenumber is simply proportional to the vertical wavenumber, so all else being
 200 equal we expect higher mode internal tides to be more susceptible to PSI. In order to apply
 201 (3) we need to know the direction of these higher-mode waves, the direction of the horizontal
 202 wave-vector.

203 Pseudomomentum is a useful quantity for assessing internal tide wave-vector direction.
 204 For a linear propagating wave, pseudomomentum is the product of the vector horizontal
 205 wavenumber and the scalar wave action,

$$206 \quad \vec{P} = k_H \vec{A} = k_H \frac{E}{\omega} \quad (7)$$

207 where k_H is the horizontal wave vector, E is the energy density, and ω the intrinsic wave
 208 frequency. For relatively low-frequency internal waves ($\omega \ll N$), this can be calculated
 209 approximately as

$$210 \quad \vec{P} \approx \left[\left\langle -\zeta \frac{du}{dz} \right\rangle, \left\langle -\zeta \frac{dv}{dz} \right\rangle \right] \quad (8)$$

211 where ζ is isopycnal displacement, u, v are eastward and northward wave velocities, and the
 212 average $\langle \rangle$ is taken over at least one wave period (Pinkel et al. 2012).

213 Pseudomomentum is calculated by applying (8) to D_2 bandpassed velocities and isopycnal
 214 displacements (as shown in Figure 5). When applied to the full D_2 fields the result is noisy.
 215 Below we show bicoherence is strongest between near-inertial waves and an internal tide
 216 at vertical scales larger than a few hundred meters. Hence D_2 signals are smoothed to
 217 200 meters vertically before pseudomomentum is calculated. Pseudomomentum time series
 218 show consistent sense of direction in different depth ranges (Fig. 5, bottom two panels). For
 219 example, eastward pseudomomentum is generally positive above 800 meters and negative
 220 below.

221 Time-averaged profiles of the eastward and northward components of \vec{P} are shown in
 222 Figure 7 (left panel), with the angle between them shown in the right panel. For propagating
 223 internal waves, the angle of the vector \vec{P} tells you the angle of the horizontal wave-vector,
 224 $\theta_k = \theta_P$. An ad-hoc estimate of the vertical wavenumber in (5), m_0 , can be calculated
 225 by doing a weighted average of vertical spectra of pseudomomentum, resulting in $m_0 \approx$
 226 $0.0074 = 2\pi/850$ meters. This is approximately the equivalent wavelength for the mode-3
 227 internal tide, the modeled fluxes for which are shown in Figure 6.

228 The time-averaged semidiurnal pseudomomentum shows two depth ranges of relatively
 229 constant angle, highlighted in grey in Figure 7. In the upper range (~ 400 - 750 m), the angle
 230 is consistent with a wave propagating slightly north of east, while in the lower depth range
 231 (~ 850 - 1250 m) the angle is consistent with a wave propagating to the northwest (compare
 232 to Fig. 6). Below we use these estimates of tidal propagation direction (θ_k) to evaluate the
 233 net energy transfer rate (5).

234 4. Evidence for PSI

235 Alford et al. (2007) discuss qualitative evidence for PSI at this site, including vertically
 236 standing near-inertial motions and the increasing prevalence of near-inertial motions with
 237 upward energy propagation equatorward of 29N. Near-inertial waves with upward energy
 238 propagation may also be generated by reflection off the bottom (Garrett 2001), though
 239 waves with the relatively small wavelengths observed here propagate very slowly, requiring
 240 very long transit times to get back to the upper ocean. In some places near-inertial waves may
 241 also be generated as lee waves by mesoscale flows over topography, though that mechanism
 242 is not predicted to be important in this part of the Pacific (Nikurashin and Ferrari 2011).

243 A more quantitative approach involves looking for evidence of phase-locking between
 244 semidiurnal and inertial motions, and ultimately applying (5) using the tide propagation
 245 direction gleaned from the pseudomomentum profiles. We start with a statistical approach

246 to look at the phasing between the three types of waves expected to participate in PSI - an
 247 internal tide, upward-going inertial waves, and downward-going inertial waves. Bandpassed
 248 time series reveal that all three types of waves show multiple wave groups present over the
 249 length of the observational record (Figs. 4, 5), and the question becomes whether there is
 250 any constant sense of phasing between them over these multiple groups.

251 The bispectrum (Kim and Powers 1979; Elgar and Guza 1988) is a measure of consistent
 252 phase relationships between triads of waves that satisfy frequency and/or wavenumber reso-
 253 nance conditions (1). Put another way, it's a method of evaluating (5) in Fourier space and
 254 determining whether there is any consistent sense of phasing between the internal tide and
 255 near-inertial waves. Bispectra are calculated as:

$$256 \quad B(\omega_1, \omega_2) = E[X_{\omega_1}^* X_{\omega_2}^* X_{\omega_1 + \omega_2}] \quad (9)$$

257 where $E[\cdot]$ is the expected value, and X represent complex FFTs of any variable of interest.
 258 Following (5), we choose the three variables to be horizontal velocity with an CW sense of
 259 rotation with depth (upward phase propagation), horizontal velocity with a CCW sense of
 260 rotation with depth (downward phase propagation), and vertical velocity. So the bispectrum
 261 as calculated here becomes

$$262 \quad B(\omega_1, \omega_2) = E[\tilde{U}_{up}^*(\omega_1) \tilde{U}_{down}^*(\omega_2) \tilde{W}(\omega_1 + \omega_2)] \quad (10)$$

263 where the tilde indicates a Fourier transform. To compute bispectra, data are divided into
 264 half overlapping 5-day windows. Fourier transforms are taken of horizontal and vertical
 265 velocity in each window, at each depth, and applied to calculate B using (10). The expected
 266 value is calculated by averaging in both depth and time. Based on the results of Figure 7
 267 that the tide has two depth ranges of reasonably consistent propagation direction, bispectra
 268 are separately depth-averaged over these two depth ranges.

269 The results are plotted as a function of ω_1, ω_2 in Figure 8 (left panels), for each of the
 270 depth ranges shown in Fig. 7. Here negative frequencies denote motions with a CW sense

271 of rotation with time. Purely inertial motions are expected to appear as $\omega=-f=-1$ cpd,
 272 while higher frequency internal waves with elliptical hodographs will bleed onto positive
 273 frequencies as well. There is a strong magnitude of the bispectrum at $(-f,-f)$, meaning
 274 potentially significant interaction between two near-inertial waves and an internal tide (twice
 275 the frequency).

276 The significance of this tendency is assessed using bicoherence, defined as

$$277 \quad b^2(\omega_1, \omega_2) = \frac{|B(\omega_1, \omega_2)|^2}{E[|X_{\omega_1} X_{\omega_2}|^2] E[|X_{\omega_1+\omega_2}|^2]} \quad (11)$$

278 where again the X s represent U_{up} , U_{down} and W respectively in our case. The bicoherence
 279 is normalized such that $0 \leq b \leq 1$. Here bicoherence is computed by taking the expected
 280 value over each indicated depth range, the result of which is shown in Fig. 8 (right panels).
 281 Elgar and Guza (1988) determine a 95% confidence level of $\sqrt{6/n_{dof}}$. Sun (2010) discusses
 282 bicoherence significance levels in some detail, and conclude that the appropriate number of
 283 degrees of freedom reflects the number of wave groups sampled, which is generally much
 284 smaller than the number of individual samples. Using a rough estimate that inertial phase
 285 and amplitude both change significantly about every 2.5 days and are coherent over about
 286 100 meters vertically (Fig. 4), we argue that the number of independent samples each of
 287 the two depth ranges used here (50 days and 350 vertical meters each) is $n_{dof} \approx 2 * 20 * 3$.
 288 This gives a 95% confidence level of 0.22. Given that the background noise level of Fig. 8
 289 appears lower, this is likely a conservative estimate. The observed bicoherences at $(-f,-f)$
 290 over this period are 0.52 for the upper depth range, and 0.54 for the lower depth range.
 291 The significance of the phase-locking between inertial and tidal motions is strong evidence of
 292 PSI and is one of the main results of this paper. In contrast, while there are other elevated
 293 regions of the bispectra, they do not appear bicoherent.

294 Bispectral techniques can also be used to look at triple product phasing in depth as well
 295 as time. In other words, bispectra can be computed as a function of vertical wavenumber
 296 in addition to frequency. Here we build on the results of frequency analysis and look at the

297 vertical wavenumber bispectra specifically between near-inertial and semidiurnal motions,

$$298 \quad B(m_1, m_2) = E[\tilde{U}_{ni}^*(m_1)\tilde{U}_{ni}^*(m_2)\tilde{W}_{D2}(m_1 + m_2)] \quad (12)$$

299 The resultant bicoherence is shown for each depth range in Figure 9 (left panels). In
300 both the upper and lower left panels there are a range of statistically significant bicoherences
301 involving waves with oppositely signed vertical wavenumbers (upper left and bottom right
302 quadrants). This is the theoretically predicted combination of up-going and down-going
303 near-inertial daughter waves. In the upper depth range the wavenumber of peak bicoherence
304 is about 0.005 (200-m wavelength), while in the lower depth range the bicoherence shifts to
305 lower wavenumbers, reflecting the larger vertical scales at depth visible in Figure 4. The
306 fact that the region of high bicoherence is close to a line with -1 slope suggests that the sum
307 wavenumber ($m_1 + m_2$) is much less than that of either daughter wave, or in other words
308 that the internal tide has larger vertical wavelengths than the inertial waves.

309 While both depth ranges indicated in Figure 9 show bicoherence between inertial and
310 tidal motions, the phase of the bispectrum is different between the two depth ranges. The
311 right panels of Figure 9 show biphas, the angle of (12), as a function of vertical wavenumber.
312 In both the upper and lower panels the biphas has a consistent sign over the wavenumber
313 range with significant bicoherence, but it is a different phase between the two panels.

314 A similar result can be seen slightly more intuitively by switching back to a time-domain
315 analysis (Sun 2010). The triple produce, Γ from (5) is computed using band passed time
316 series of up-going near-inertial horizontal velocity, down-going near-inertial horizontal veloc-
317 ity, and semidiurnal vertical velocity. All time series have been vertically low-passed below
318 0.02cpm, as suggested by the regions of bicoherence in Figure 9. The absolute value and
319 complex phase of Γ are shown in Figure 10. Between about 400 and 800 meters depth, there
320 are three pulses of $|\Gamma|$ near year days 120,135 and 150 that roughly line up with the spring
321 tides in the top panel of Figure 5. In regions with strong magnitude of Γ (black contour),
322 the angle is of one sense above about 800 meters depth (blue) and of another sign below
323 (red).

324 In fact, given that the internal tide has a different propagation direction in these two
325 depth ranges (Fig. 7), one would expect the biphase to have a different sign in each depth
326 range, through (5). The final step is to fully evaluate (5) combining the time-domain triple
327 product, Γ and the tidal propagating angle, θ_k estimated from pseudomomentum. The result
328 is plotted in the bottom panel of Figure 10. Remarkably, it is positive almost everywhere,
329 arguing for a steady energy transfer from the internal tide to near-inertial waves. The major
330 exception, below 800 meters between yeardays 145 and 150, is a time with a strong upward
331 phase / downward energy packet visible in Figure 4, which could be a wind generated wave.

332 The overall positive magnitude of (5) seen in Figure 10 requires that the complex phase
333 of Γ be balanced by the phase term in (5) related to tidal propagation (6). This can be seen
334 explicitly by comparing the average angles, as done in the left panel of Figure 11. Given the
335 complexities of the wave field at this location, they are in remarkably good agreement, with
336 both showing consistent signs in the two depth ranges indicated. The time averaged rate
337 of energy transfer is shown in the right panel. This is the estimated rate of energy transfer
338 from the internal tide to near-inertial motions through PSI, and is the second major result
339 of this paper. For reference, the average turbulent dissipation rate calculated by MacKinnon
340 et al. (2012) is also shown.

341 5. Discussion and Conclusions

342 The two most robust result of this work are 1) that there is a consistent, statistically
343 bicoherent sense of phase between the internal tide and near-inertial waves as would only
344 be expected when PSI is present, and 2) that the particular sense of that phase is one that
345 leads to positive energy transfer from the internal tide to near-inertial waves.

346 The data show two depth ranges that have relatively consistent sense of semidiurnal
347 pseudomomentum (Fig. 7). In each of these depth ranges, bispectral calculations in both
348 frequency and wavenumber space show statistically significant phase-locking between three

349 participating waves - an up-going near-inertial wave, a down-going near-inertial wave, and a
350 semidiurnal internal tide. Using the tidal direction as estimate from pseudomomentum we
351 calculate a net positive energy transfer from the internal tide to near-inertial daughter waves
352 (Fig. 11). Though several previous studies have documented phase locking using bispectra
353 (Carter and Gregg 2006; Sun 2010), to our knowledge this is the first study to explicitly
354 calculate the energy transfer rates using an equation like (5).

355 As always with this type of calculation, care must be taken to not falsely conflate diur-
356 nal motions produced by PSI with those from either wind-generated waves or the diurnal
357 internal tide. Wind generated waves would be expected to have primarily downward energy
358 propagation (Alford et al. 2012). Diurnal internal tides would likely have similar vertical
359 scales as the semidiurnal internal tides, not the high-mode structure of the diurnal motions
360 discussed here. Most importantly, it is extremely unlikely that either wind or tidally gen-
361 erated diurnal motions would create features with exactly the right phase locking with the
362 semidiurnal internal tide to indicate PSI.

363 The calculated magnitude of the energy transfer rate is quite modest, of roughly the
364 same order as the local dissipation rates presented in the companion paper (Fig. 11). A
365 rough timescale for subharmonic growth rate is given by the ratio of inertial energy (Fig.
366 4) to the tendency term, $\tau \sim E_{ni}/(dE/dt)$. Taking the average either up- or down-going
367 energy for E_{ni} and energy transfer rates from Fig. 11 gives timescales for growth of 2-5 days.
368 Our estimate of the magnitude of the energy transfer rate is significantly more uncertain,
369 reflecting uncertainty in all terms going into (5). One of the biggest uncertainties in the
370 difficulty in estimating the direction of horizontal internal tide propagation direction in a
371 complex wave field. When multiple waves are present with different propagation direction,
372 the linear polarization relations and their byproducts (energy flux or pseudomomentum)
373 become very difficult to interpret in a simple way (Nash et al. 2006; Martini et al. 2011).

374 The emerging story is that while PSI does befall a propagating internal tide, it does not
375 do so in the catastrophic way predicted by MW. Hazewinkel and Winters (2011) argue that

376 the timescales for PSI growth are not much faster than the spring-neap cycle, so that truly
377 catastrophic growth effectively can't occur in any given spring tide. Based upon the results
378 presented here, we believe that explanation is probably supplemented by the reasoning that
379 1) it is not mode-1 but closer to mode-3 internal tides that dominate energy transfer through
380 PSI at this location, 2) these waves have geographically complex flux patterns that are likely
381 to change with the evolving mesoscale as waves refract, 3) timescales for PSI growth (2-
382 5 days from these estimates) are comparable to typical synoptic timescales of mesoscale
383 evolution. Truly catastrophic PSI growth simply doesn't have time to take hold. Further
384 numerical simulations with more complex internal tide forcing, or observational studies in a
385 location with a simpler internal tide, may provide further insight.

386 Jochum (2009) argues that even a moderate elevation associated with PSI at some lat-
387 itudes may be an important mixing pattern to include in global models. Nevertheless, our
388 results argue that the majority of internal tide energy escapes to dissipate in distant grave-
389 yards, the search for which is still ongoing.

390 *Acknowledgments.*

391 This work was sponsored by NSF OCE 04-25283. We thank the tireless captain and crew
392 of the R/V Revelle, for making our two months at sea productive and enjoyable. Eric
393 Boget, Andrew Cookson played an essential role in the design, construction, deployment
394 and recovery of the moorings. Tom Peacock, Paula Echeverri, and Kim Martini provided
395 valuable assistance at sea. Shaun Johnston and Ed Zaron graciously conducted numerical
396 simulations for our experiment. Many members of an ongoing ocean mixing Climate Process
397 Team provided useful feedback and suggestions.

REFERENCES

- 400 Alford, M. H., 2008: Observations of parametric subharmonic instability of the diurnal
401 internal tide in the South China Sea. *Geophys. Res. Lett.*, **35** (L15602), doi:
402 10.1029/2008GLO34720.
- 403 Alford, M. H., 2010: Sustained, full-water-column observations of internal waves and mixing
404 near Mendocino Escarpment. *J. Phys. Oceanogr.*, **40**, 2643–2660.
- 405 Alford, M. H., M. F. Cronin, and J. M. Klymak, 2012: Annual cycle and depth penetration
406 of wind-generated near-inertial internal waves at Ocean Station Papa in the Northeast
407 Pacific. *J. Phys. Oceanogr.*, (**in press**).
- 408 Alford, M. H., J. A. MacKinnon, Z. Zhao, R. Pinkel, J. Klymak, and T. Peacock, 2007:
409 Internal waves across the Pacific. *Geophys. Res. Lett.*, **34** (doi:10.1029/2007GL031566).
- 410 Carter, G. S. and M. C. Gregg, 2006: Persistent near-diurnal internal waves observed above
411 a site of M_2 barotropic-to-baroclinic conversion. *J. Phys. Oceanogr.*, **36** (6), 1136–1147.
- 412 Doherty, K., D. Frye, S. Liberatore, and J. Toole, 1999: A moored profiling instrument. *J.*
413 *Atmos. Ocean. Tech.*, **16**, 1816–1829.
- 414 Elgar, S. and R. T. Guza, 1988: Statistics of bicoherence. *IEEE Trans. Acous., Speech,*
415 *Signal Proc.*, **36**, 1667–1668.
- 416 Garrett, C., 2001: What is the “Near-Inertial” band and why is it different from the rest of
417 the internal wave spectrum? *J. Phys. Oceanogr.*, **31**, 962–971.
- 418 Garrett, C. and E. Kunze, 2007: Internal tide generation in the deep ocean. *Ann. Rev. of*
419 *Fluid Mech.*, **39**, 57–87, doi: 10.1146/annurev.fluid.39.050905.110227.

420 Gregg, M. C., T. B. Sanford, and D. P. Winkel, 2003: Reduced mixing from the breaking of
421 internal waves in equatorial waters. *Nature*, **422**, 513–515.

422 Harrison, M. and R. Hallberg, 2008: Pacific subtropical cell response to reduced equatorial
423 dissipation. *J. Phys. Oceanogr.*, **38 (9)**, 1894–1912.

424 Hazewinkel, J. and K. Winters, 2011: Psi of the internal tide on a -plane: Flux divergence
425 and near-inertial wave propagation. *J. Phys. Oceanogr.*, **41 (9)**, 1673–1682.

426 Jayne, S. R., 2009: The impact of abyssal mixing parameterizations in an ocean general
427 circulation model. *J. Phys. Oceanogr.*, **39**, 1756–1775.

428 Jochum, M., 2009: Impact of latitudinal variations in vertical diffusivity impact of latitudinal
429 variations in vertical diffusivity on climate simulations. *J. Geophys. Res.*, **114 (C01010)**,
430 **doi:10.1029/2008JC005030**,).

431 Kim, Y. and E. Powers, 1979: Digital bispectral analysis and its application to nonlinear
432 wave interactions. *IEEE Trans. Plasma Sci.*, **PS-7 (120-131)**.

433 Leaman, K. D. and T. B. Sanford, 1976: Observations on the vertical polarization and energy
434 flux of near-inertial waves. *J. Geophys. Res.*, **6**, 894–908.

435 Lueck, R. G. and J. J. Picklo, 1990: Thermal inertia of conductivity cells: Observations with
436 a Sea-Bird cell. *J. Atmos. Ocean. Tech.*, **7**, 756–768.

437 MacKinnon, J. A., M. H. Alford, R. Pinkel, J. Klymak, and Z. Zhao, 2012: The latitudinal
438 dependence of shear and mixing in the Pacific transiting the critical latitude for PSI. *J.*
439 *Phys. Oceanogr.*, **submitted**.

440 MacKinnon, J. A. and K. Winters, 2005: Subtropical catastrophe: significant loss
441 of low-mode tidal energy at 28.9 degrees. *Geophysical Research Letters*, **32 (15)**,
442 **doi:10.1029/2005GL023376**.

443 Martini, K. I., M. H. Alford, E. Kunze, S. H. Kelly, and J. D. Nash, 2011: Observations of
444 internal tides on the Oregon continental slope. *J. Phys. Oceanogr.*, **41** (9), 1772–1794.

445 McComas, C. H., 1977: Resonant interaction of oceanic internal waves. *J. Geophys. Res.*,
446 **82** (9), 1397–1412.

447 Müller, P., G. Holloway, F. Henyey, and N. Pomphrey, 1986: Nonlinear interactions among
448 internal gravity waves. *Rev. Geophys.*, **24** (3), 493–536.

449 Nash, J. D., E. Kunze, C. M. Lee, and T. B. Sanford, 2006: Structure of the baroclinic tide
450 generated at Kaena Ridge, Hawaii. *J. Phys. Oceanogr.*, **36**, 1123–1135.

451 Nikurashin, M. and R. Ferrari, 2011: Global energy conversion rate from geostrophic flows
452 into internal lee waves in the deep ocean. *Geophys. Res. Lett.*, **38**, 10.1029/2011GL046576.

453 Nycander, J., 2005: Generation of internal waves in the deep ocean by tides. *J. Geophys.*
454 *Res.*, **110**, doi:10.1029/2004JC002487.

455 Olbers, D. J., 1983: Models of the oceanic internal wave field. *Rev. Geophys. Space Physics*,
456 **21** (7), 1567–1606.

457 Pickering, A., M. Alford, Z. Zhao, J. MacKinnon, R. Pinkel, and J. Klymak, 2012: Near-
458 inertial waves during the Internal Waves Across the Pacific Experiment, in prep.

459 Pinkel, R., L. Rainville, and J. Klymak, 2012: Semidiurnal baroclinic wave momentum fluxes
460 at Kaena Ridge, Hawaii. *J. Phys. Oceanogr.*, **42** (8), 1249–1269.

461 Rainville, L. and R. Pinkel, 2006: Propagation of low-mode internal waves through the
462 ocean. *J. Phys. Oceanogr.*, **36** (6), 1220–1236, submitted.

463 Simmons, H. L., 2008: Spectral modification and geographic redistribution of the semi-
464 diurnal internal tide. *Ocean Modelling*, **21**, 126–138.

- 465 Sun, O., 2010: Subharmonic energy transfer from the semidiurnal internal tide at Kaena
466 Ridge. Ph.D. thesis, UCSD.
- 467 Young, W., Y. Tsang, and N. Balmforth, 2008: Near-inertial parametric subharmonic insta-
468 bility. *J. Fluid Mech.*, **607**, 25–49, submitted.
- 469 Zhao, Z. and M. H. Alford, 2009: New altimetric estimates of mode-one M2 internal tides
470 in the Central North Pacific Ocean. *jpo*, **39**, 1669–1684.
- 471 Zhao, Z., M. H. Alford, J. A. MacKinnon, and R. Pinkel, 2010: Long-range propagation
472 of the semidiurnal internal tide from the Hawaiian Ridge. *J. Phys. Oceanogr.*, **40** (4),
473 713–736.

474 List of Figures

- 475 1 Bathymetry (colors; axis at lower right), measurement locations (black, moorings;
476 white, ship track), and internal-tide energy fluxes (black, altimetry estimates from
477 Zhao and Alford (2009); red, mooring estimates from Zhao et al. (2010)). Reference
478 arrows are at upper left; the M_2 critical latitude, 28.8N, is indicated with a dotted
479 line. 23
- 480 2 Velocity in the east-west (upper) and north-south (lower) directions from the MP3
481 mooring, in a semi-Lagrangian (isopycnal following) reference frame. The yearday
482 convention is such that noon on 1 January is yearday 0.5. 24
- 483 3 Depth-averaged spectra of potential energy (black), horizontal kinetic energy with
484 upward going phase (downward energy, red), and horizontal kinetic energy with
485 downward going phase (upward energy, blue) as a function of frequency. Inertial
486 and semidiurnal (M_2 , S_2) frequencies are indicated for reference by vertical grey lines 25
- 487 4 Top: northward component of band passed near-inertial velocity. Middle: the com-
488 ponent of near-inertial velocity that rotates CW with depth, which according to the
489 linear internal wave polarization relations should be consistent with motions that
490 propagate upward in time, as visible in the figure. Bottom: near-inertial velocity
491 that that rotates CCW with depth, consistent with downward phase propagation. 26
- 492 5 Top: magnitude of barotropic velocity at the mooring side, smoothed over 2 days.
493 Next three panels: bandpassed semidiurnal eastward velocity, northward velocity,
494 and vertical displacement, respectively. Bottom two panels are the northward and
495 eastward component of pseudomomentum. 27

496	6	Depth-integrated tidal energy fluxes from the POM model for mode-3 . The model was initiated with horizontally uniform stratification and forced with a barotropic tide over approximately the region shown in Fig. 1. Scale arrows in upper right. The red diamond marks the location of the MP3 mooring. Grey shaded contours indicate water depth, with seamounts visible to the north and east of the mooring. Courtesy of T.M.S. Johnston.	28
497			
498			
499			
500			
501			
502	7	Left: time-averaged profiles of the eastward (black) and northward (red) components of vector pseudomomentum (8). Right: angle of vector pseudomomentum, θ_P . In the text this angle is used as a proxy for the angle of internal tide propagation, $\theta_k \approx \theta_P$ in (5).	29
503			
504			
505			
506	8	Left panels: absolute value of the bispectrum , as given by (10), for upper and lower depth ranges indicated in Figure 7 (note the log scale for the colorbar). Right panels: bicoherence for same depth ranges.	30
507			
508			
509	9	Left panels: bicoherence as a function of vertical wavenumber for (-f,-f,D2) frequency product for upper and lower depth ranges indicated in Figure 7 (note the log scale for the colorbar). Right panels: biphas for same depth ranges.	31
510			
511			
512	10	Complex phase (top) and absolute value (middle) of the triple product Γ from (5). Bottom panel is the full energy transfer term from (5) , where Γ has been multiplied by the phase term with the tidal direction given by pseudomomentum, $\theta_k \approx \theta_P$	32
513			
514			
515	11	Left: comparison of expected and calculated triple product phase. Red line shows the negative of the angle of the calculated triple product, Γ in (5), while the black line shows the angle term in (5) using the direction of the semidiurnal pseudomomentum as a proxy for the internal tide propagation direction. The agreement means that the product of the two terms in (5) is positive definite, leading to net positive energy transfer. Right: time-averaged magnitude of energy transfer calculated using (5), in blue. Also shown is the average dissipation rate profile (red), reproduced from MacKinnon et al. (2012).	33
516			
517			
518			
519			
520			
521			
522			

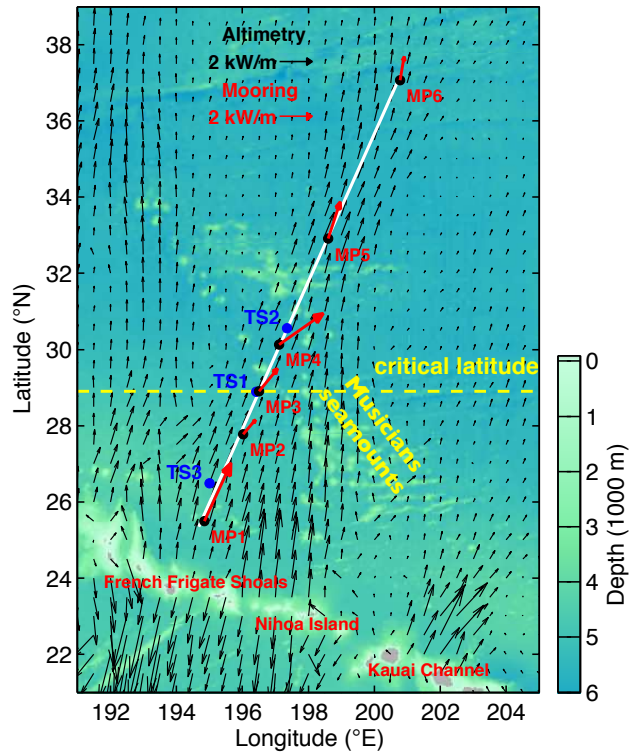


FIG. 1. Bathymetry (colors; axis at lower right), measurement locations (black, moorings; white, ship track), and internal-tide energy fluxes (black, altimetry estimates from Zhao and Alford (2009); red, mooring estimates from Zhao et al. (2010)). Reference arrows are at upper left; the M_2 critical latitude, 28.8N, is indicated with a dotted line.

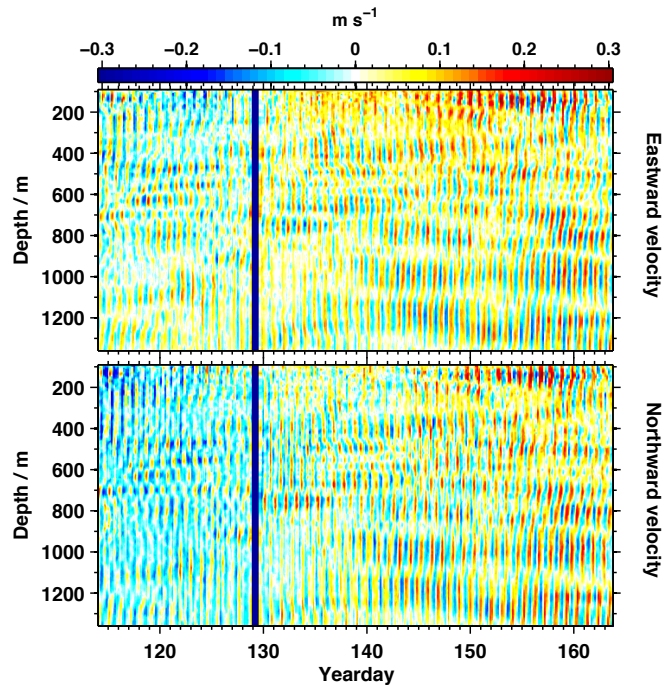


FIG. 2. Velocity in the east-west (upper) and north-south (lower) directions from the MP3 mooring, in a semi-Lagrangian (isopycnal following) reference frame. The yearday convention is such that noon on 1 January is yearday 0.5.

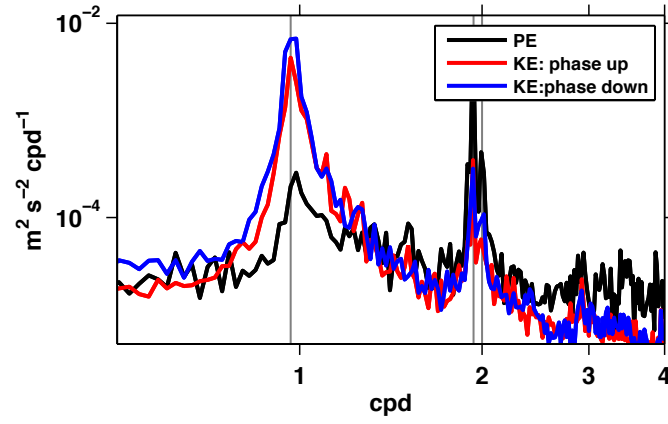


FIG. 3. Depth-averaged spectra of potential energy (black), horizontal kinetic energy with upward going phase (downward energy, red), and horizontal kinetic energy with downward going phase (upward energy, blue) as a function of frequency. Inertial and semidiurnal (M_2 , S_2) frequencies are indicated for reference by vertical grey lines

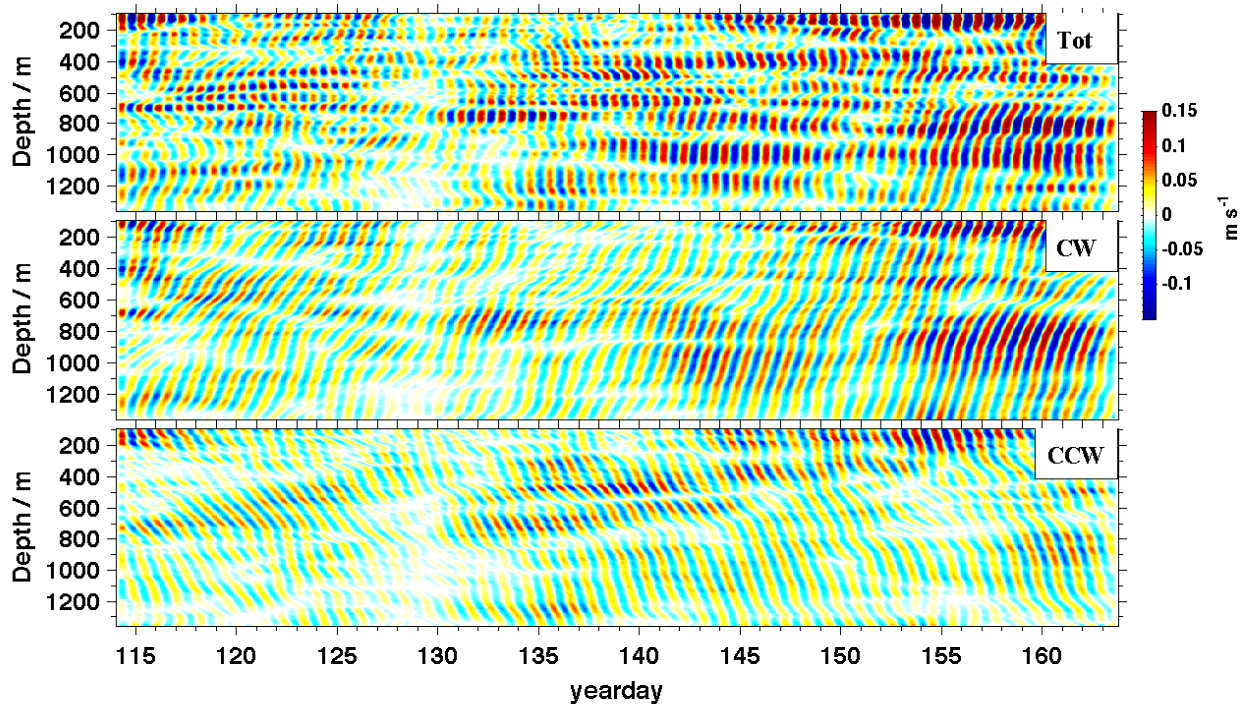


FIG. 4. Top: northward component of band passed near-inertial velocity. Middle: the component of near-inertial velocity that rotates CW with depth, which according to the linear internal wave polarization relations should be consistent with motions that propagate upward in time, as visible in the figure. Bottom: near-inertial velocity that that rotates CCW with depth, consistent with downward phase propagation.

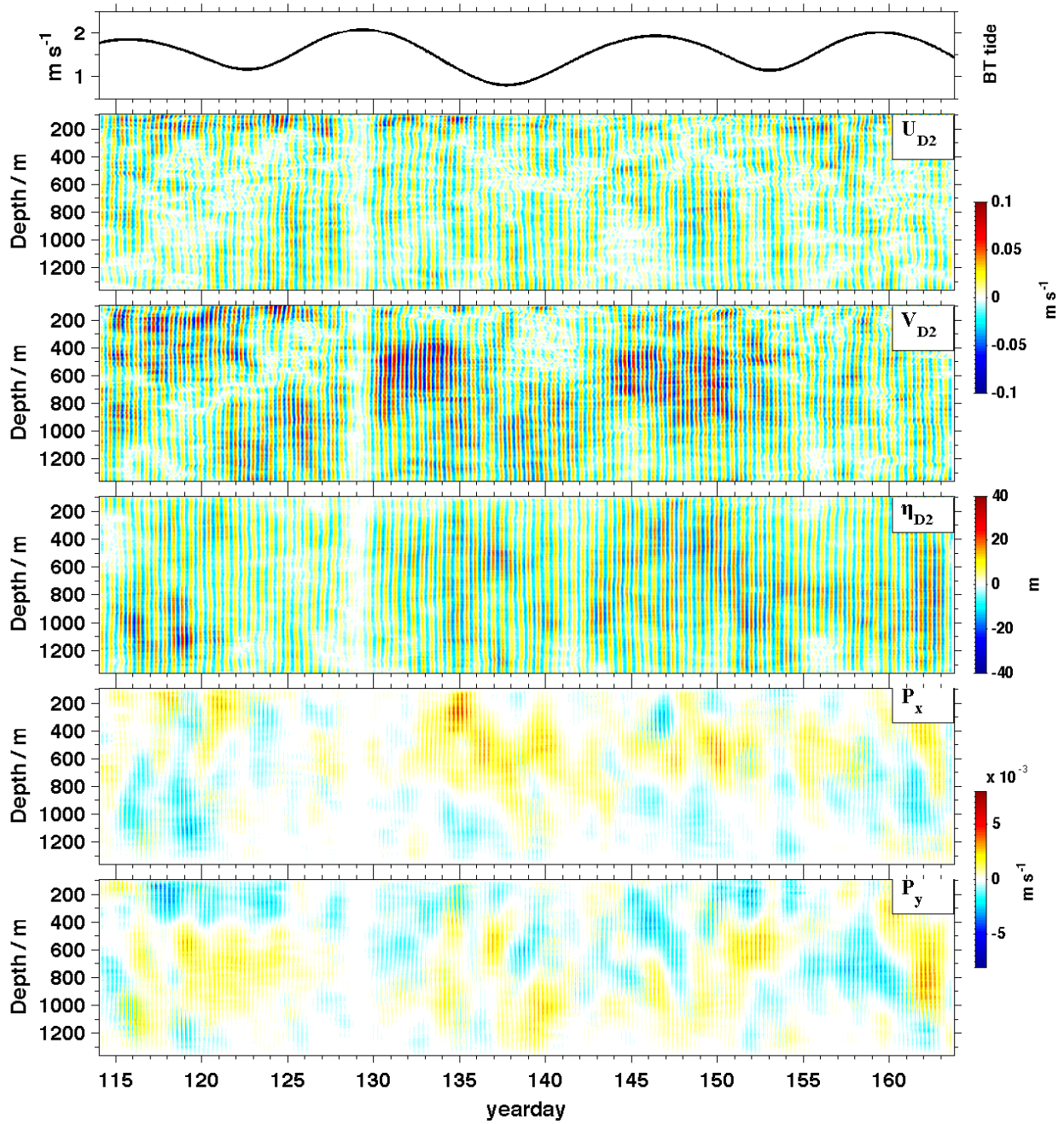


FIG. 5. Top: magnitude of barotropic velocity at the mooring side, smoothed over 2 days. Next three panels: bandpassed semidiurnal eastward velocity, northward velocity, and vertical displacement, respectively. Bottom two panels are the northward and eastward component of pseudomomentum.

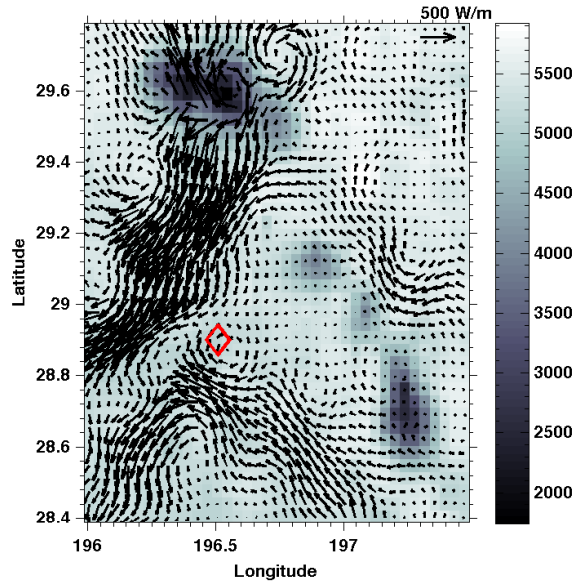


FIG. 6. Depth-integrated tidal energy fluxes from the POM model for mode-3 . The model was initiated with horizontally uniform stratification and forced with a barotropic tide over approximately the region shown in Fig. 1. Scale arrows in upper right. The red diamond marks the location of the MP3 mooring. Grey shaded contours indicate water depth, with seamounts visible to the north and east of the mooring. Courtesy of T.M.S. Johnston.

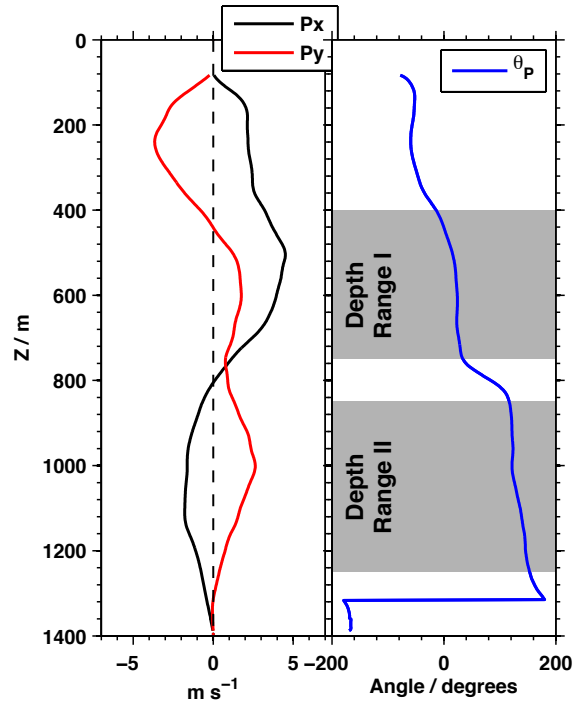


FIG. 7. Left: time-averaged profiles of the eastward (black) and northward (red) components of vector pseudomomentum (8). Right: angle of vector pseudomomentum, θ_P . In the text this angle is used as a proxy for the angle of internal tide propagation, $\theta_k \approx \theta_P$ in (5).

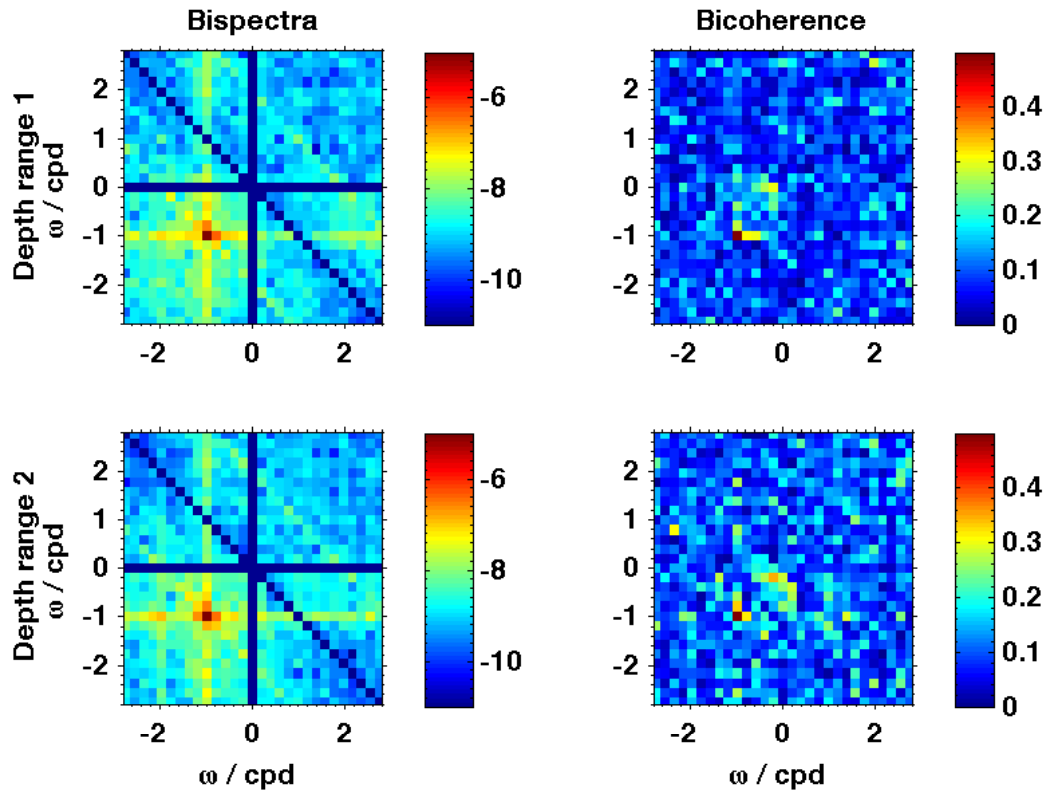


FIG. 8. Left panels: absolute value of the bispectrum, as given by (10), for upper and lower depth ranges indicated in Figure 7 (note the log scale for the colorbar). Right panels: bicoherence for same depth ranges.

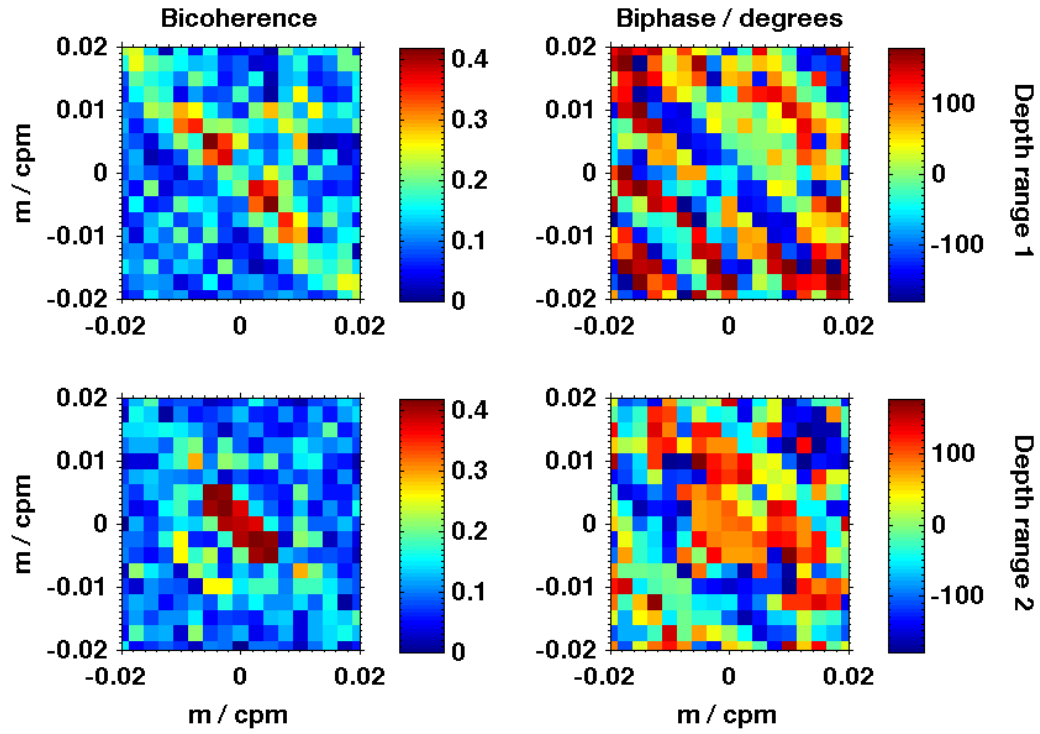


FIG. 9. Left panels: bicoherence as a function of vertical wavenumber for $(-f,-f,D2)$ frequency product for upper and lower depth ranges indicated in Figure 7 (note the log scale for the colorbar). Right panels: biphaseness for same depth ranges.

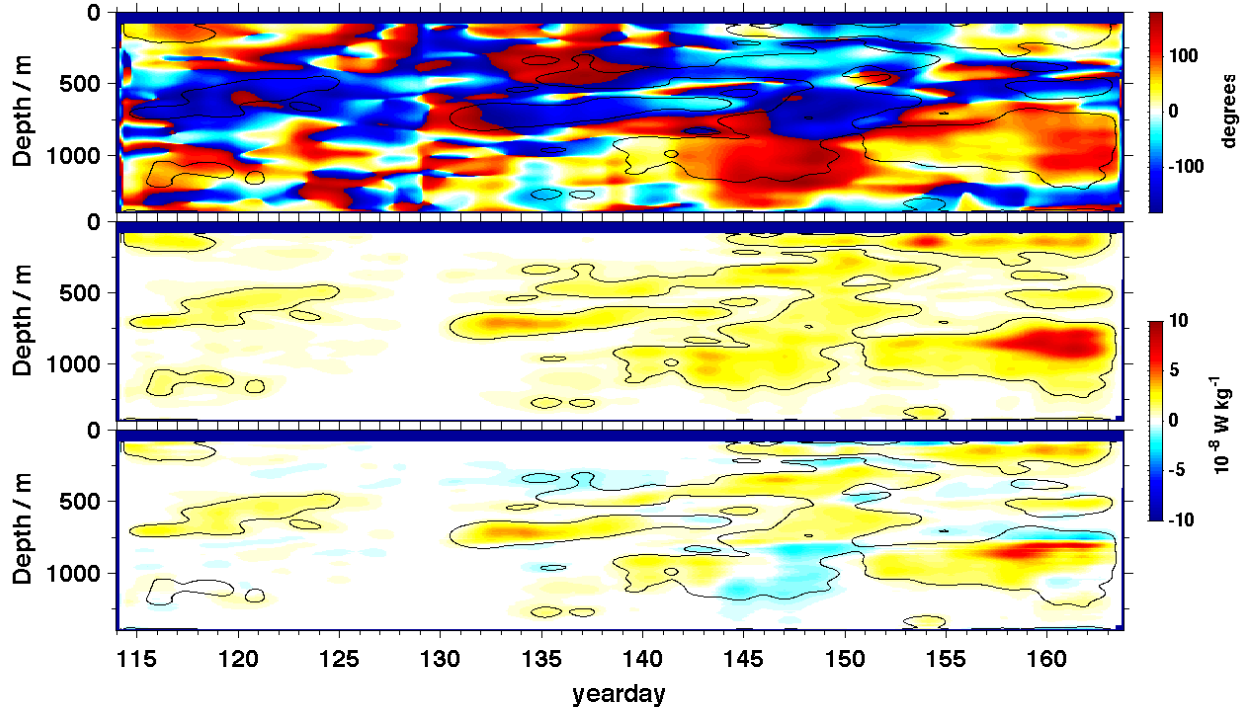


FIG. 10. Complex phase (top) and absolute value (middle) of the triple product Γ from (5). Bottom panel is the full energy transfer term from (5), where Γ has been multiplied by the phase term with the tidal direction given by pseudomomentum, $\theta_k \approx \theta_P$

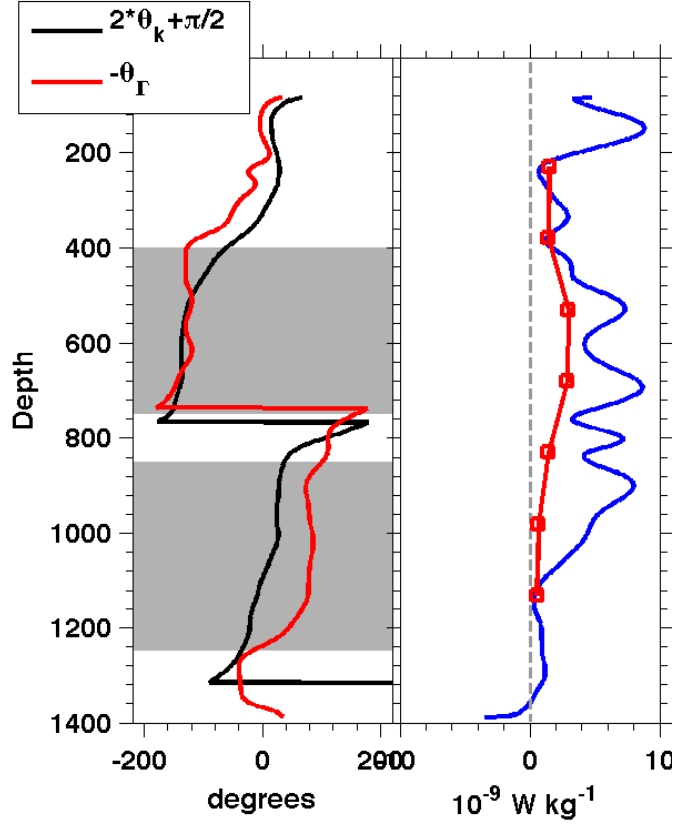


FIG. 11. Left: comparison of expected and calculated triple product phase. Red line shows the negative of the angle of the calculated triple product, Γ in (5), while the black line shows the angle term in (5) using the direction of the semidiurnal pseudomomentum as a proxy for the internal tide propagation direction. The agreement means that the product of the two terms in (5) is positive definite, leading to net positive energy transfer. Right: time-averaged magnitude of energy transfer calculated using (5), in blue. Also shown is the average dissipation rate profile (red), reproduced from MacKinnon et al. (2012).